Responses to Reviewer #1

This manuscript presents a valuable multi-year, high-temporal-resolution dataset of permafrost ground-surface deformation from the central Tibetan Plateau. The combination of 5-min LVDT measurements, ultrasonic ranging, GNSS-IR, Sentinel-1 InSAR, and soil hydrothermal observations provides a relatively unique opportunity to examine ground deformation across sub-daily to multi-year timescales. In particular, the high-frequency LVDT observations have the potential to improve our understanding of deformation processes that are difficult to resolve using conventional field measurements or satellite observations. However, several methodological and interpretational issues need to be addressed before the main conclusions can be adequately supported.

We thank the reviewer for the valuable and constructive comments. We appreciate the recognition of the value of the observation record. These comments have helped us improve the assessment of measurement accuracy and uncertainty, strengthen the reliability of our process interpretations, and improve the comparison among monitoring methods. Our point-by-point responses are provided below.

Major comments:

1. The uncertainty of the LVDT measurements needs to be evaluated much more carefully, particularly because some of the sub-daily deformation signals interpreted in the manuscript are very small. The stated sensor resolution does not directly represent measurement accuracy, and possible effects from instrumental noise, thermal expansion/contraction, and benchmark stability should be quantified before sub-millimetre deformation is interpreted physically.

Thank you very much for this comment. We have made two revisions to better assess the precision and accuracy of the LVDT measurements:

1) We added a 35 h indoor warming experiment to assess the sensor's temperature dependence. Temperature and displacement were recorded at approximately 1 min intervals, yielding 1984 observations for evaluating the sensor's temperature response and measurement precision. The results are presented in Appendix Figure A2.

As shown in Figure A2(a), the temperature increased from approximately −25 to 20 °C over 35 h, while the measured displacement increased from approximately 0 to 0.37 mm. Displacement exhibited an approximately linear relationship with temperature (Figure A2(b)), with a fitted slope of 0.00831 ± 0.00004 mm °/C (1σ) and an R^2 of 0.9640 for 1984 observations. During the relatively stable temperature interval of 19.00–19.80 °C

shown in Figure A2(c), 194 valid observations were available. The readings were confined to two data values separated by 0.010 mm, consistent with a reading repeatability of 0.010 mm.

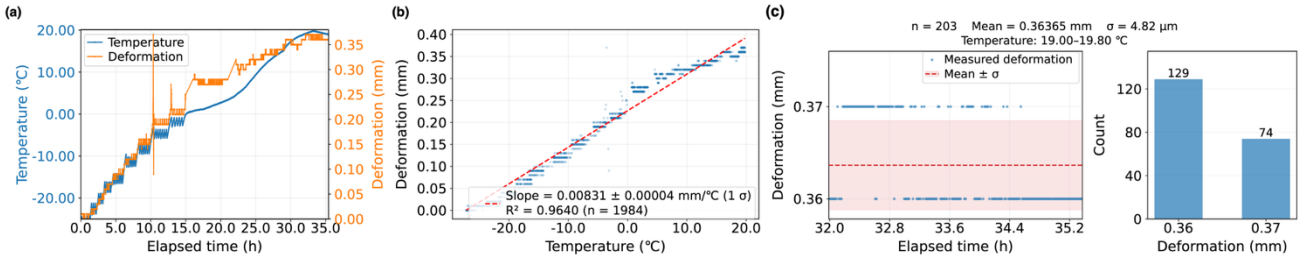


Figure A2. Temperature response of the LVDT sensor during a 35 h indoor warming experiment, with measurements recorded at approximately 1 min intervals. (a) Time series of temperature and measured displacement. (b) Relationship between temperature and measured displacement, with the linear regression fit shown by the red dashed line. (c) Displacement time series (left) and frequency distribution (right) during the final test interval at 19.0–19.8 °C. The measurements obtained under these relatively stable temperature conditions are consistent with the sensor's specified repeatability of 0.01 mm.

The sensor's measurement precision is described in the main text as follows:

The LVDT sensor used in this study has a measurement range of 150 mm, a linearity error of ≤ 0.25 % of full scale, and a manufacturer-specified repeatability of 0.01 mm. Indoor tests indicate that the measured displacement increases by 0.00831 mm for each 1 °C rise in temperature (Appendix Figure A2). Applying this sensitivity to the recorded daily mean air temperature range of −28.41 to 11.31 °C yields an estimated temperature-induced displacement range of approximately 0.33 mm. Given the relatively small magnitude of this estimate even across such a wide temperature range, potential errors associated with thermal expansion and contraction of the sensor assembly were not explicitly corrected.

2) We also analyzed field observations during a winter interval when the soil was fully frozen and actual ground surface deformation was expected to be small, to help assess the observational noise of the complete system under field conditions. The example for 14–18 May 2024 previously shown in Figure 9 has been replaced with the interval of 1–5 March 2024, for which the soil temperature and moisture profiles indicate fully frozen conditions. The corresponding statements in the manuscript reads are as follows:

4.3.5 Negligible net displacement during late freezing (LF-2023–24: 20240301–20240305)

Between 1 and 5 March 2024, the LVDT record showed negligible net displacement (−0.01 mm), despite discernible diurnal oscillations with daily peak-to-peak ranges of 0.06–0.17 mm (Fig. 9a-5). The mean diurnal cycle reached a maximum around 06:00 and a minimum around 13:00. Soil temperatures at all measured depths

remained below 0 °C throughout the period. At 5 cm depth, temperature ranged from −13.0 to −0.8 °C, and volumetric water content ranged from 0.013 to 0.085 m^3/m^3. Period-mean volumetric water contents were less than 0.11 m^3/m^3 at all measured depths below 5 cm. At 220 and 240 cm, temperatures remained between −3.3 and −1.5 °C and between −3.2 and −1.7 °C, respectively. The LVDT sensor's measured temperature sensitivity of 0.00831 mm/°C suggests that its temperature-dependent response may have contributed to the small diurnal oscillations, although the available observations cannot conclusively distinguish this response from actual ground movement. On 4 March, the daily temperature range at 5 cm was only 2.9 °C, and the deformation range was 0.06 mm, both smaller than on the other four days. These observations under fully frozen soil conditions also provide a qualitative check on the precision of the LVDT measurements. The negligible net displacement indicates relatively stable ground surface elevation during this late-freezing interval.

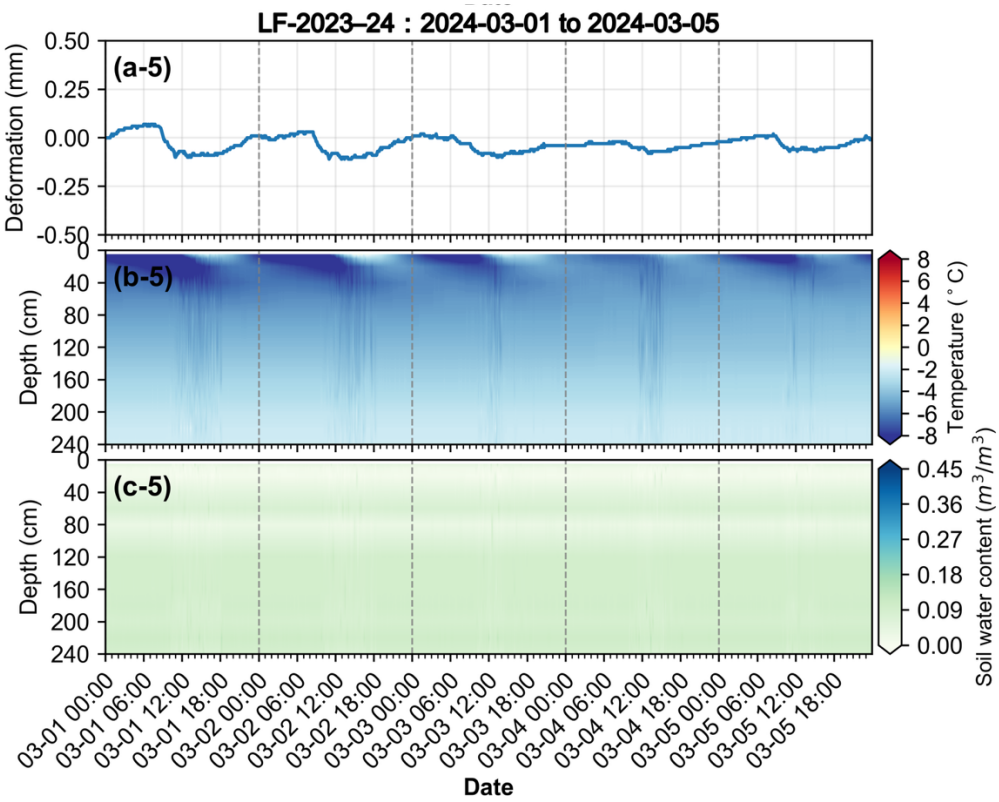


Figure 9(a-5, b-5, c-5). Representative sub-daily ground surface deformation, together with the corresponding soil temperature and moisture profiles. Panel a present ground surface deformation at 5 min resolution, with the time series shifted so that the value at the first time step is zero. Panel b and c show soil temperature and soil moisture profiles, respectively, at 10 min resolution.

2. The representativeness of the LVDT measurements also needs further consideration. The LVDT measures deformation over an approximately 8-cm footprint, while vegetation conditions around the footplate appear substantially different between summer and winter, and the manuscript does not clearly demonstrate whether

vegetation growth, surface contact, or local microtopography can affect the measurement. More importantly, it is unclear whether deformation measured at such a small footprint can reasonably represent the much larger footprints of GNSS-IR and particularly the 40–80 m scale represented by InSAR. This scale mismatch should be explicitly evaluated rather than treating the four measurements as directly comparable.

Thank you very much for this comment.

1) We have clarified the differences in observational footprint among the monitoring methods. Table 1 summarizes the observational footprint and temporal sampling interval of each method used in this study.

Table 1. Information on in-situ LVDT-based, ultrasonic ranging, GNSS-IR and Sentinel-1 InSAR monitoring of ground deformation.

Observation	**Observation footprint (diameter)**	**Observation interval**	**Time step used for analysis**
LVDT-based measurement	8 cm	5 min	5 min and 1 d
Ultrasonic ranging	~1 m	10 min	1 d
GNSS-IR	~50 m	1 s	1 d
Sentinel-1 SBAS-InSAR	~30 m (10 × 2 multilooking, incidence angle of 43.13°)	12 days for Sentinel-1 SAR acquisitions, with occasional 24-day intervals	12 d (occasionally 24 d)

2) Figure 2 shows the vegetation and snow conditions surrounding the LVDT sensor in summer and winter. We have also added the mass of the LVDT footplate and explained how its weight provides a downward preload that helps maintain contact with the ground surface. The revised text reads: “The perforated footplate has a mass of approximately 258 g, providing a downward load of approximately 2.53 N that helps maintain contact with the ground surface. This contact-based configuration reduces sensitivity to changes in vegetation canopy and snow surface height, although mechanical effects of vegetation beneath or around the plate have not been independently quantified.”

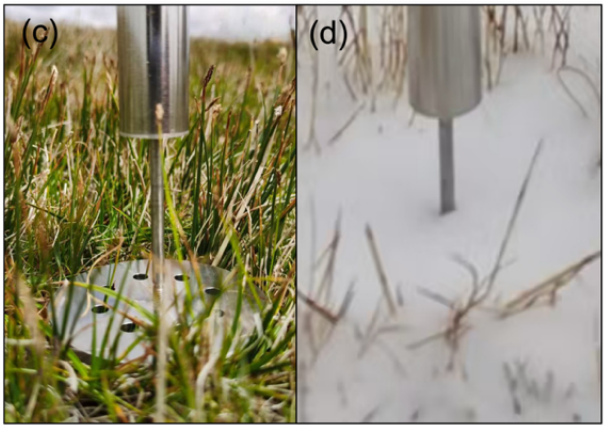


Figure 2(c–d). Enlarged views of the sensor footplate in summer and winter. The footplate rests on a flat ground surface.

3) We have emphasized differences in sensor footprint and the implications of spatial heterogeneity for interpreting and comparing the observations.

In **Section 4.2 Intercomparison of multi-sensor ground surface deformation records**, we have added the following statement:

Figure 7 shows the four deformation records (LVDT, GNSS-IR, ultrasonic ranging, and InSAR) together with the corresponding meteorological and soil hydrothermal profiles at SLC03. Despite substantial differences in sensor footprint and noise level, all methods capture the seasonal freeze–thaw cycle and the progressive subsiding of the ground surface from 2022 to 2025.

Despite the similarities between LVDT and InSAR in deformation patterns, multiannual trends, and seasonal deformation, differences remain in the apparent timing of freeze–thaw deformation. The native InSAR sampling interval of approximately 12 d and temporal smoothing limit the precision of onset estimates. Nevertheless, Figure 7a shows that sustained thaw settlement begins later in the LVDT record than in the InSAR record, particularly at SLC03. This discrepancy may partly reflect differences in spatial support (~30 m for InSAR versus 0.08 m for LVDT; Table 1), combined with surface heterogeneity and differences in local soil conditions. At the onset of sustained LVDT settlement at SLC03, the thaw front depths estimated by interpolating the soil temperature profiles are already 61.4 cm, 85.1 cm, and 85.8 cm on 27 May 2023, 1 June 2024, and 19 May 2025, respectively. The depth-weighted mean volumetric water content in the upper 60 cm during late May (20–31 May) is 0.085 m^3/m^3, 0.116 m^3/m^3, and 0.083 m^3/m^3 in 2023, 2024, and 2025, respectively. The two nearby soil sensor arrays (less than 10 m apart) also record contrasting shallow soil moisture conditions. During 20–31

May in 2023–2025, depth-weighted mean volumetric water content in the upper 10 cm ranges from 0.080 to 0.101 m^3/m^3 in the newer array and from 0.173 to 0.225 m^3/m^3 in the older array. These observations suggest that relatively dry shallow soil and pronounced soil moisture heterogeneity may contribute to the delayed onset of sustained settlement at the LVDT measurement point and to differences among the monitoring methods.

4) We have expanded the Discussion to explain how differences in spatial scale can contribute to discrepancies among deformation measurements from different sensors.

LVDT has a very small effective footprint and captures point-scale deformation. Differences in spatial scale should therefore be considered when comparing LVDT with InSAR, which represents spatially averaged deformation over scales of approximately 10–100 m, or GNSS-IR, which has a footprint of approximately 50 m. In heterogeneous surface environments, observations with larger footprints integrate deformation across multiple microtopographic and subsurface settings, each characterized by different thawing and freezing onset times and seasonal amplitudes. The superposition of these local deformation processes smooths the signal and can obscure process-level features captured at a single point. Our comparison of LVDT and InSAR records shows that, although the two generally agree in long-term deformation trends and seasonal deformations, discrepancies remain in the onset and cessation of frost heave and thaw settlement (Figure 7a) and in seasonal amplitude in individual years. For example, during the 2023–2024 freeze–thaw cycle at SLC07, the LVDT record shows a marked increase in seasonal amplitude, whereas the InSAR-derived seasonal amplitude remains comparable to those of preceding years (Appendix Figure A4, shown below the responses to question 3).

At SLC07, both frost heave and thaw subsidence were substantially greater following higher precipitation in 2023 and a possible local increase in soil water content, resulting in a much larger seasonal deformation amplitude during the 2023–2024 freeze–thaw cycle. In contrast, the InSAR-derived seasonal deformation over an approximately 30 m footprint differed little between the 2023–2024 cycle and other years. These contrasting observations highlight pronounced spatial heterogeneity in ground surface deformation.

3. The multi-sensor comparison needs to be redesigned more rigorously. As shown in Figure 7, the deformation series can be referenced to a common starting date, whereas some of the subsequent comparisons appear to retain different offsets or reference conditions. More importantly, the very high correlations among the four

datasets are somewhat misleading because all records contain a strong common seasonal cycle and long-term trend. A high Pearson correlation therefore does not necessarily indicate measurement agreement. The authors should compare the datasets over exactly the same time period and reference date and evaluate differences in magnitude, seasonal amplitude, trend, and residual deformation in addition to correlation.

Thank you for this important suggestion. All deformation records in Figure 7 are now referenced to 18 June 2022 to remove initial offsets among the instruments. In addition to Pearson correlation coefficients, seasonal amplitudes, and long-term trends, we have included bias, MAE, and RMSE. The revised text in **Section 4.2 Intercomparison of multi-sensor ground surface deformation records** is as follows:

To further quantify the agreement and discrepancies among the four monitoring records at SLC03, we compare the records on common dates. The InSAR vertical displacement time series is linearly interpolated to a daily time grid, while the other three records retain their original daily values. The comparison is restricted to 841 common valid dates between 18 June 2022 and 13 August 2025, and all records are referenced to 18 June 2022. Each deformation time series is fitted with a model combining a linear trend and an annual sinusoidal term to estimate the multiannual deformation trend and seasonal peak-to-peak deformation. All four methods indicate persistent ground surface subsidence at SLC03, with multiannual trends of −14.9 mm yr^{-1} for LVDT, −19.7 mm yr^{-1} for InSAR, −32.7 mm yr^{-1} for ultrasonic ranging, and −38.2 mm yr^{-1} for GNSS-IR (Figure 8a). The LVDT record shows the largest seasonal deformation (69.3 mm), followed by InSAR (60.9 mm), GNSS-IR (44.0 mm), and ultrasonic ranging (35.6 mm; Figure 8b). Across all common dates, the LVDT record correlates most strongly with InSAR (r = 0.85), with a root mean square error (RMSE) of 13.02 mm and a mean absolute error (MAE) of 11.15 mm (Figure 8c–f). Its correlations with GNSS-IR and ultrasonic ranging are weaker (r = 0.58 and 0.57, respectively), with corresponding RMSEs of 46.19 mm and 53.26 mm and MAEs of 39.51 mm and 48.37 mm (Figure 8c–f). During the November–May periods (382 common dates), the LVDT–InSAR correlation is 0.81, whereas the LVDT correlations with GNSS-IR and ultrasonic ranging are 0.46 and 0.33, respectively (Figure 8g). During the June–October periods (459 common dates), the corresponding correlation coefficients are 0.83, 0.66, and 0.66 (Figure 8h). GNSS-IR and ultrasonic ranging remain strongly correlated across the full record and both seasonal subsets (r = 0.93–0.97), with an overall RMSE of 13.61 mm and an MAE of 10.95 mm. Overall, LVDT and InSAR show closer agreement in their multiannual trends and seasonal deformation ranges, while GNSS-IR and ultrasonic ranging also closely resemble each other.

A separate comparison at SLC07 yields an InSAR-LVDT correlation of 0.71, an RMSE of 20.0 mm, and a bias of −14.5 mm (Figure A4). During the 2023–2024 freeze–thaw cycle, the LVDT record shows a marked increase in seasonal deformation range, whereas the InSAR record does not exhibit a similarly pronounced change. Agreement is particularly close over the 31 paired SAR acquisition dates from 12 November 2021 to 19 November 2022, with r = 0.98, an RMSE of 7.06 mm, and an MAE of 6.33 mm.

Despite the similarities between LVDT and InSAR in deformation patterns, multiannual trends, and seasonal deformation, differences remain in the apparent timing of freeze–thaw deformation. The native InSAR sampling interval of approximately 12 d and temporal smoothing limit the precision of onset estimates. Nevertheless, Figure 7a shows that sustained thaw settlement begins later in the LVDT record than in the InSAR record, particularly at SLC03. This discrepancy may partly reflect differences in spatial support (~30 m for InSAR versus 0.08 m for LVDT; Table 1), combined with surface heterogeneity and differences in local soil conditions. At the onset of sustained LVDT settlement at SLC03, the thaw front depths estimated by interpolating the soil temperature profiles are already 61.4 cm, 85.1 cm, and 85.8 cm on 27 May 2023, 1 June 2024, and 19 May 2025, respectively. The depth-weighted mean volumetric water content in the upper 60 cm during late May (20–31 May) is 0.085 m^3/m^3, 0.116 m^3/m^3, and 0.083 m^3/m^3 in 2023, 2024, and 2025, respectively. The two nearby soil sensor arrays (less than 10 m apart) also record contrasting shallow soil moisture conditions. During 20–31 May in 2023–2025, depth-weighted mean volumetric water content in the upper 10 cm ranges from 0.080 to 0.101 m^3/m^3 in the newer array and from 0.173 to 0.225 m^3/m^3 in the older array. These observations suggest that relatively dry shallow soil and pronounced soil moisture heterogeneity may contribute to the delayed onset of sustained settlement at the LVDT measurement point and to differences among the monitoring methods. In addition, the InSAR-derived deformation signal may be affected by snow accumulation and melt. Repeated snowfall and snowmelt during the early thaw season (Figure 5) may therefore also contribute to the earlier apparent onset of settlement in the InSAR record compared with the LVDT record.

The larger subsidence trends derived from GNSS-IR and ultrasonic ranging may reflect pronounced local thaw settlement associated with installation disturbance within their observation footprints. This interpretation is consistent with the thermokarst ponds and localized subsidence observed around the instrument foundations (Figure A5). Differences in benchmark stability may also contribute. The LVDT reference rods are anchored to depths of 30 m at SLC03 and 20 m at SLC07, whereas the foundations supporting the GNSS antenna and

ultrasonic ranging sensor are anchored to a depth of 6 m. Structural movement, including frost jacking, cannot be ruled out and is discussed further in Section 5.1.

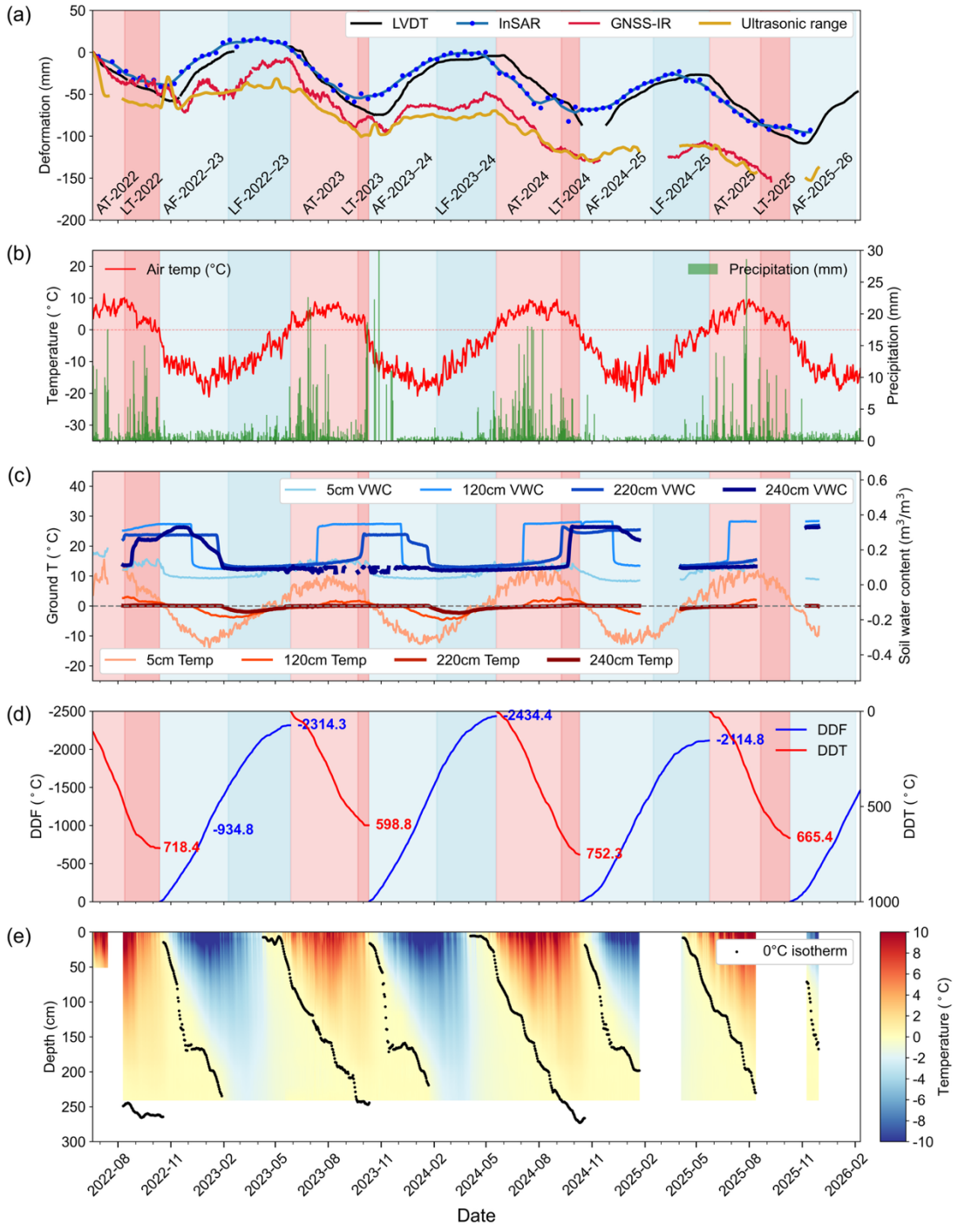


Figure 7. Multi-sensor ground surface deformation and hydrothermal conditions at the SLC03 supersite during 2022–2026. (a) Ground surface deformation time series derived from LVDT, Sentinel-1 SBAS-InSAR, GNSS-IR, and ultrasonic ranging. The deformation time series from different observation methods were referenced to 18 June 2022. Shaded blue and red bands indicate freezing and thawing stages, respectively. Light red and red represent Active layer thawing (AT) and Late-summer thawing (LT), and light blue and blue represent Active

layer freezing (AF) and Late-winter freezing (LF). (b) Daily air temperature and precipitation. (c) Soil temperature and volumetric water content at 5, 120, 220, and 240 cm depth. (d) degree days of thawing (DDT) and degree days of freezing (DDF). (e) Soil temperature profile; the black dot indicates the estimated 0 °C isotherm based on soil temperature profile.

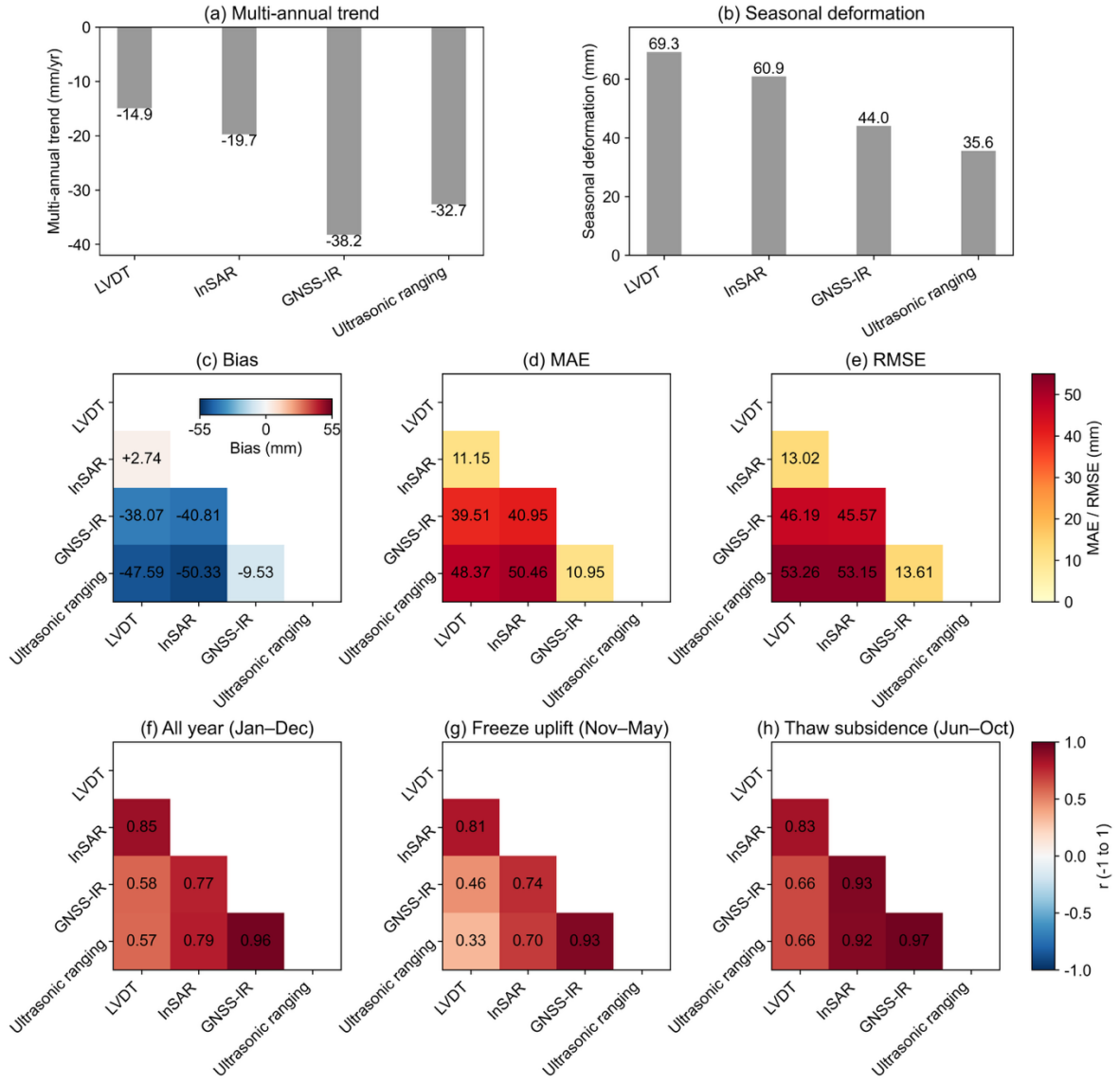


Figure 8. Intercomparison of ground surface deformation records from four monitoring methods at the SLC03 supersite. (a) Multiannual subsidence trends and (b) seasonal peak-to-peak deformation derived from LVDT, Sentinel-1 InSAR, GNSS-IR, and ultrasonic ranging. Pairwise (c) bias, (d) MAE, and (e) RMSE, all expressed in millimetres. Bias is calculated as the record on the vertical axis minus that on the horizontal axis. Pairwise Pearson correlation coefficients for (f) the full observation period, (g) the frost-heave period (November–May), and (h) the thaw-settlement period (June–October).

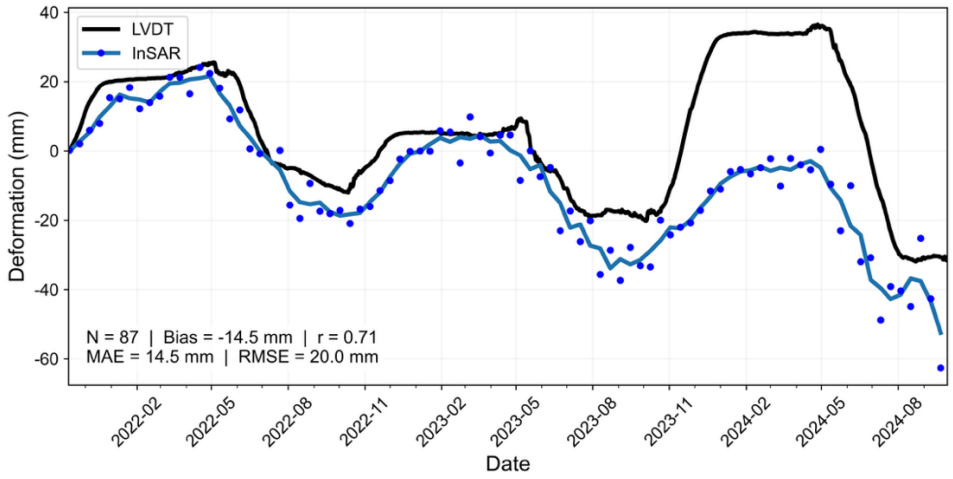


Figure A4. Comparison of LVDT and Sentinel-1 InSAR vertical deformation time series at SLC07. The black line shows the LVDT record, blue dots represent individual InSAR observations, and the blue line shows the smoothed InSAR series. Summary statistics are calculated from 87 paired observations, with bias defined as InSAR minus LVDT.

4. The statement that changes in active-layer water content can explain more than 78% of the seasonal deformation is not physically clear. The manuscript appears to relate changes in measured volumetric liquid water content to surface deformation, but liquid-water-content changes during freezing and thawing cannot directly be converted into vertical ground deformation without considering soil porosity, ice segregation, water migration, soil compressibility, and the volume change associated with phase transition. The calculation and its physical assumptions need to be fully explained and justified; otherwise, this quantitative conclusion should be removed or substantially weakened.

Thank you very much for pointing out this issue. In Section 4.4.1, we have added a description of the calculation and its limitations. We have removed the quantitative attribution of 78% from the Abstract and Conclusions. In the Abstract, this attribution has been replaced with a qualitative statement emphasizing the strong statistical association between active-layer water content and seasonal deformation. Figure 10b has also been revised to illustrate this relationship. The revised statement describes ice–water phase change within the active layer as an important driver of seasonal ground surface deformation. The revised text in **Section 4.4.1 Deformation characteristics across freeze–thaw stages based on the LVDT measurements** is as follows:

Figure 10b shows the differences in depth-weighted mean volumetric water content over 0–240 cm and monthly mean surface deformation between March and September, representing frozen- and thaw-season conditions, respectively. When March data are unavailable, February or April is used instead. September is selected to represent conditions when the thaw front approaches the base of the active layer. This comparison is intended

to emphasize deformation associated with active layer freeze–thaw processes while limiting the influence of drainage and consolidation following the thaw of ground ice at the top of permafrost. From the frozen-season month (March, or February or April when March data are unavailable) to September in 2023 and 2024, water content increases by 0.191–0.216 m^3/m^3, accompanied by surface subsidence of 51.7–62.8 mm. From September to the following frozen-season reference month during 2022–2025, water content decreases by 0.181–0.211 m^3/m^3, accompanied by surface heave of 32.1–54.4 mm. To assess the magnitude of ground surface deformation expected from ice–water phase transitions within the active layer, we assume that the observed water content changes arise entirely from phase transitions and that the associated volume changes are fully expressed as vertical deformation. Ice segregation, water migration, and soil compressibility are not considered. Using a thawing or freezing depth of 2.4 m (although thaw depths are greater in warm years) and assuming approximately 9 % volumetric expansion of water upon freezing, we estimate phase-change deformation magnitudes of 39.2–46.7 mm, equivalent to 74 %–122 % of the observed seasonal deformation magnitudes. After removal of the linear subsidence trend from the deformation records, seasonal deformation magnitudes range from 40.0 to 61.3 mm, and the phase-change estimates are equivalent to 74 %–98 % of these detrended magnitudes.

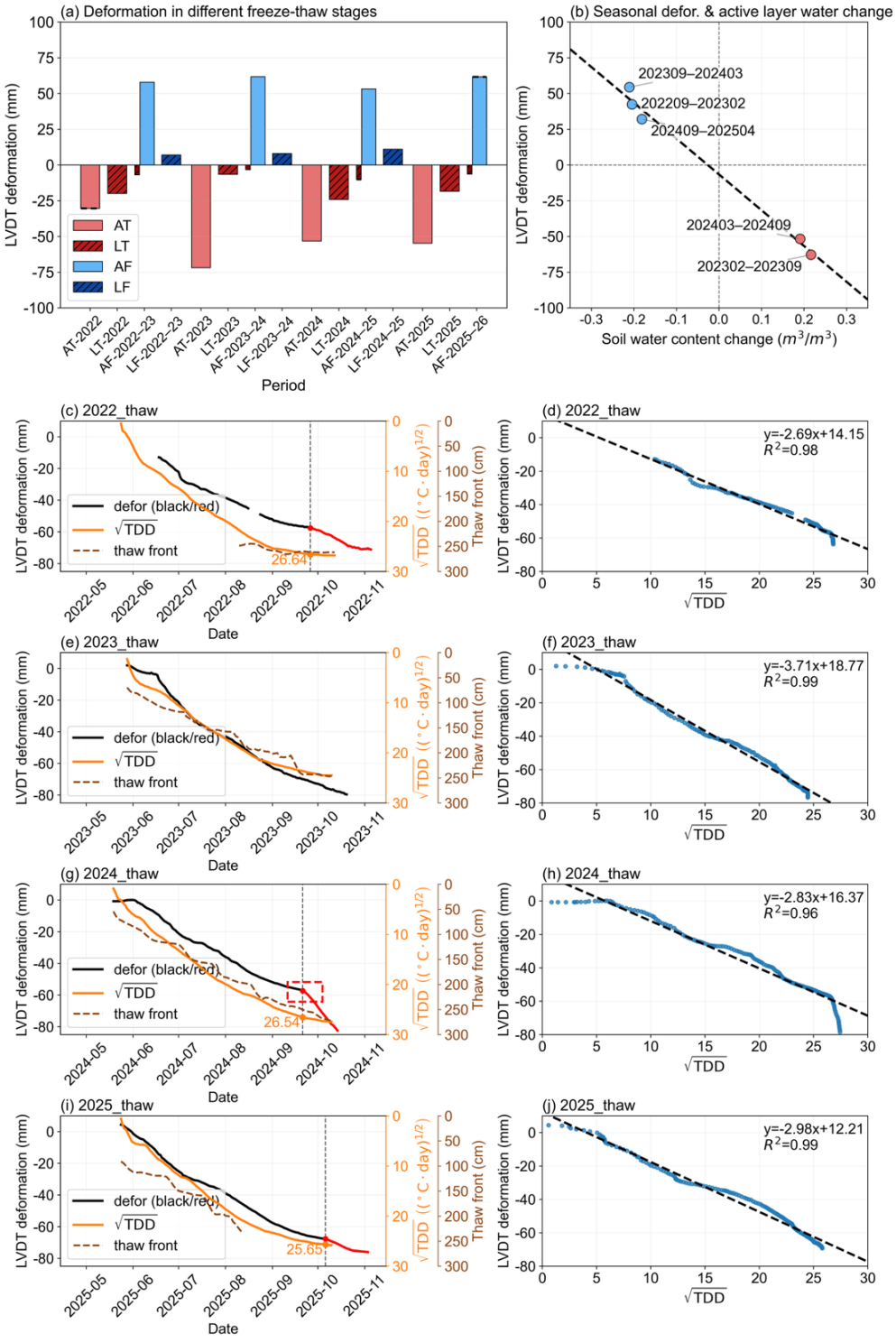


Figure 10. Deformation characteristics across freeze-thaw stages and their relationships with thaw progression. (a) Deformation partitioned into active thaw (AT), late thaw (LT), active freezing (AF), and late freezing (LF) stages for different annual cycles. (b) Seasonal deformation and active layer water content change. (c, e, g, i) Deformation curves, $\sqrt{\text{TDD}}$, and thaw-front depth during the thaw seasons of 2022, 2023, 2024, and 2025. For ease of intercomparison, the deformation time series was shifted such that the deformation was approximately zero at $\sqrt{\text{TDD}} = 5$. Black and red segments indicate deformation before and after the late-season breakpoint, respectively. Orange numbers at the base of the orange lines in (c), (g), and (i) indicate the √TDD values corresponding to the deformation breakpoints. No breakpoint was detected in 2023 (e), the coldest of the four

years. (d, f, h, j) Relationships between thaw-season deformation and $\sqrt{\mathrm{TDD}}$ for the corresponding years, together with linear regressions.

5. There is currently no clear evidence demonstrating that the observed late-season breakpoint acceleration is caused by excess ground-ice melt. The increase in soil moisture at depth and the simultaneous acceleration in subsidence are consistent with deeper thaw, but they do not distinguish thaw of excess ground ice from thaw of ordinary pore ice or subsequent consolidation and drainage processes. Unless independent borehole or cryostratigraphic observations demonstrate excess ice at the corresponding depth, the interpretation should be presented as a possible mechanism rather than direct evidence.

Thank you for this suggestion. To better support the interpretation that the thaw front reaches an ice-rich layer at the top of permafrost in exceptionally warm years, we have made the following revisions:

1) We have added descriptions of borehole-core observations at SLC03 and SLC07, together with field measurements of the soil water content (ground ice) profile at different depths. The added text in Section 2 Study Area is as follows:

2 Study area and measurement sites

Borehole drilling conducted during the Second Tibetan Plateau Scientific Expedition in November 2019 provided the foundation for subsequent permafrost observations. By this time of year, seasonal thaw is generally expected to have reached its maximum depth. The 2019 field records document contrasting surface conditions at the two sites. Site SLC03 occupies a flat valley floor supporting alpine swamp meadow, with approximately 90 % vegetation cover, locally degraded frost-heave hummocks, and exposed gravel. SLC07 is situated in degraded alpine meadow with sparse vegetation, a dry, sandy surface containing gravel, and pronounced soil salinization. The boreholes reach depths of 30 m at SLC03 and 20 m at SLC07. At SLC03, the drilling log describes fine sand with gravel in the upper meter, underlain by gravelly sand between 1.0 and 4.6 m depth, tentatively interpreted as glaciofluvial deposits. Ice crystals are visible at 2.4–3.0 m, and the core recovered from 3.0–4.5 m contains abundant water and has a slurry-like consistency. Discrete ice layers occur at greater depths, including an approximately 2.5 mm thick layer within 4.6–5.1 m, a 2.8 cm thick pure-ice layer at 7.3–7.4 m, and a 30 cm thick pure-ice layer at 16.0–16.3 m. Volumetric water content in borehole core samples from SLC03 varied substantially across depths of 0.2–29.4 m, with a mean of 0.32 m^3/m^3 and particularly high values of 0.47 and 0.56 m^3/m^3 at 2.7 and 4.6 m, respectively (Appendix Figure A1). Subsequent active layer temperature and moisture profiles indicate an active layer thickness (ALT) of approximately 2.4 m. Together

with the drilling records, these observations suggest the presence of excess ice near the top of permafrost. At SLC07, the drilling log describes dry sandy soil at 0–0.7 m, clay at 0.7–1.6 m, and rock at 1.6–3.5 m. Abundant liquid water was observed in the fragmented core recovered from 2.5–3.5 m. Clay containing angular rock fragments occurs at 3.5–6.0 m, where liquid water but no visible ice was recorded. Rock dominates the 6.0–18.0 m interval, with liquid water noted at 6.0–6.5 m, whereas grey clay containing gravel occurs at 18.0–20.0 m, with no visible ice recorded. Volumetric water contents at depths of approximately 0.5, 1.2, and 3.5 m are 0.31, 0.42, and 0.27 m^3/m^3, respectively.

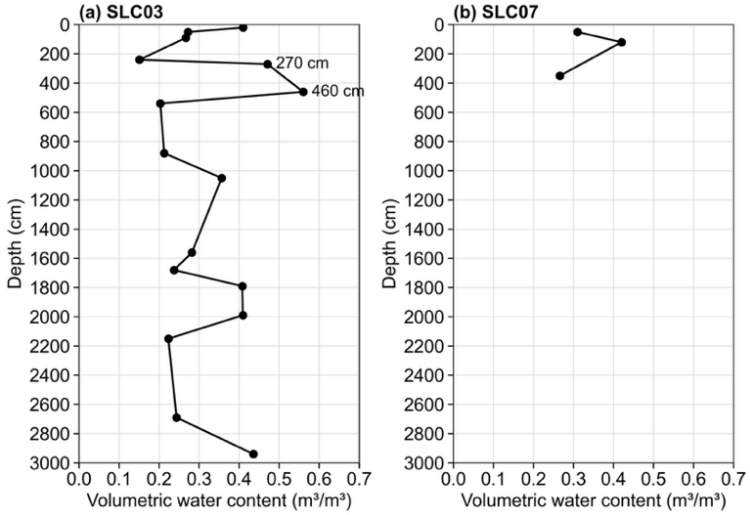


Figure A1. Volumetric water content profiles from borehole core samples collected at (a) SLC03 and (b) SLC07. Black circles denote values at sampling depths.

2) We have also estimated annual maximum thaw depths from the soil temperature and moisture profiles. In Section 3.5 Meteorological and active layer hydrothermal monitoring, we have added the method for estimating daily 0 °C isotherm depths and revised Figure 7e to show more clearly the differences between the cool year (2023) and the warm years (2022 and 2024). Using 20 November–10 December as the annual comparison window, mean volumetric water content at 240 cm was 0.317, 0.098, 0.331, and 0.329 m^3/m^3 in 2022, 2023, 2024, and 2025, respectively. The soil moisture profiles suggest that thaw likely did not reach 240 cm in 2023, whereas they clearly indicate thawing at this depth in 2022 and 2024 (Figure 7c). Extrapolation of the soil temperature profiles suggests maximum thaw depths of approximately 260 cm in 2022 and 2024, at least 20 cm greater than in 2023 (Figure 7e). Together with the borehole observations, these results suggest an ALT of approximately 2.4 m and the presence of excess ice near the top of permafrost at SLC03, supporting the interpretation that the thaw front reaches an ice-rich layer in exceptionally warm years.

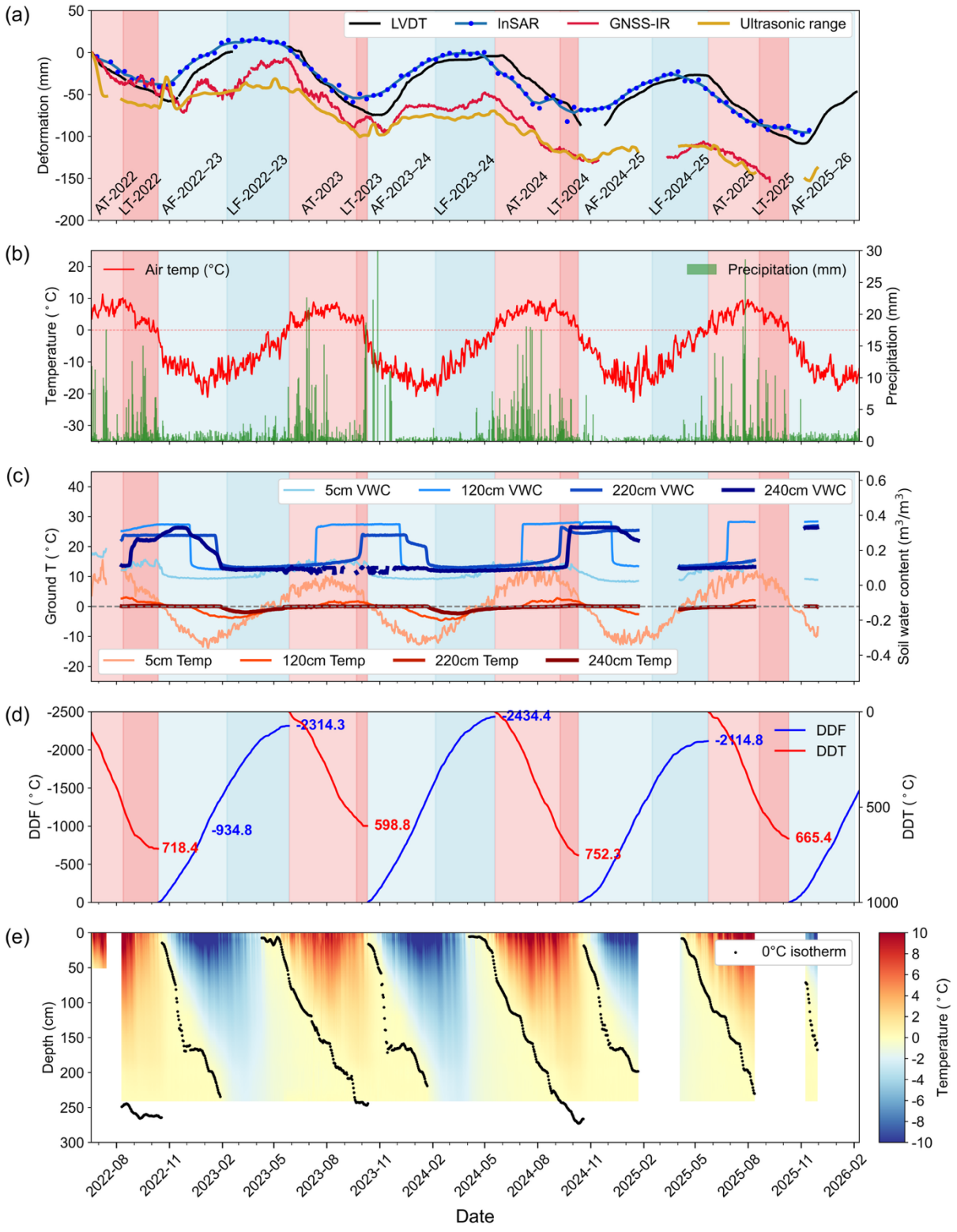


Figure 7. Multi-sensor ground surface deformation and hydrothermal conditions at the SLC03 supersite during 2022–2026. (a) Ground surface deformation time series derived from LVDT, Sentinel-1 SBAS-InSAR, GNSS-IR, and ultrasonic ranging. The deformation time series from different observation methods were referenced to 18 June 2022. Shaded blue and red bands indicate freezing and thawing stages, respectively. Light red and red represent Active layer thawing (AT) and Late-summer thawing (LT), and light blue and blue represent Active layer freezing (AF) and Late-winter freezing (LF). (b) Daily air temperature and precipitation. (c) Soil

temperature and volumetric water content at 5, 120, 220, and 240 cm depth. (d) degree days of thawing (DDT) and degree days of freezing (DDF). (e) Soil temperature profile; the black dot indicates the estimated 0 °C isotherm based on soil temperature profile.

6. More generally, several process interpretations in the manuscript are stronger than the observations support. The sub-daily observations are interesting and potentially very useful, but the manuscript should more clearly distinguish what is directly observed from what is inferred from temporal coincidence between deformation, temperature, and soil moisture. A more cautious interpretation would strengthen rather than weaken the contribution of this dataset.

Thank you for this suggestion. The original manuscript interpreted three deformation processes: late-thaw-season subsidence associated with excess ground ice melt, infiltration and refreezing during the April heave event, and diurnal deformation during the early thaw season.

(1) Following the reviewer's suggestion and considering the sensor's temperature dependence, we have removed the interpretation of diurnal frost-heave deformation, as its magnitude of approximately 0.1 mm is comparable to the temperature-induced displacement. We have instead focused on the other two mechanisms and provided additional evidence to support their interpretation.

(2) To support the interpretation of late-thaw-season breakpoint-style acceleration, we have added cryostratigraphic evidence for the presence of excess ice at the top of permafrost at the observation site. We have also described the interpolation and extrapolation methods for estimating 0 °C isotherm depths in the Methods section. These estimates, together with the soil moisture profiles, support the interpretation that the thaw front reached the ice-rich layer.

(3) To better explain slight early-spring heave and the refreezing of infiltrated water, we have expanded Section 4.4.3. Following Reviewer 2's suggestion, we have moved Figure A3 from the Appendix to this section, where it is now Figure 12. We have also refined the figure, incorporated snow depth observations, and extended the analysis from 16–20 April 2024 to 16–30 April 2024. The longer interval includes additional heave events associated with snow accumulation and subsequent melt, with supporting evidence from shallow soil temperature and moisture profiles.

The revised figure and accompanying text are provided below:

4.4.3 Late-freezing slight heave and refreezing of infiltrated water

Small but distinct heave events are observed at both sites between mid-April and early May, including at SLC03 in 2024 and 2025 and at SLC07 in 2022–2024 (Figure 4). Figure 9a-6 illustrates the detailed deformation time series during 16–20 April 2024 at SLC03. The deformation progresses through discrete, rapid upward steps separated by short plateaus, contrasting with the smoother winter uplift observed during other periods (e.g., Figure 9a-3 and a-4).

Figure 12 extends this analysis to 30 April 2024, combining the deformation record with soil temperature and moisture observations in the upper 20 cm and ultrasonic snow depth estimates. Five upward steps are identified in Figure 12a: 0.18 mm at approximately 15:00 on 16 April, 0.30 mm at approximately 17:00 on 17 April, 0.32 mm at approximately 08:20 on 22 April, 0.44 mm at approximately 17:15 on 25 April, and 0.22 mm at approximately 10:40 on 29 April. Four of these five steps occur on the same day as, or the day after, snow depth increases recorded by ultrasonic ranging (Figure 12b). Snow depth increases relative to the preceding day by 6.82 mm, 42.90 mm, 3.53 mm, and 5.51 mm on 16, 17, 24, and 28 April, respectively. Snow accumulation on these days is followed by decreases in snow depth, consistent with subsequent snowmelt. The heave events also coincide with, or follow, shallow soil warming and increases in soil moisture. Daily maximum temperatures at 5 cm reach 3.7 °C on 16 April and 3.8 °C on 24 April. Volumetric water content at 5 cm is elevated around these events compared with values on nearby dates, with daily maxima reaching approximately 0.09 m^3/m^3 on 16 April and 0.10–0.13 m^3/m^3 on 21–22, and 24–25 April. During some heave events, however, diurnal soil temperature fluctuations are suppressed. On 17 April, temperature variations at 5 cm are damped, with a daily minimum of −1.1 °C and a maximum of 0.0 °C; the temperature remains nearly constant at approximately −0.1 °C from 18:00 to 22:00, rather than exhibiting the usual diurnal oscillation. Temperature fluctuations on 25 April are also smaller than on the preceding days. Such temperature stabilization near the freezing point may reflect latent heat released during refreezing. Together, the snow depth changes, elevated shallow soil moisture, suppressed temperature fluctuations, and stepwise heave support the interpretation of snowmelt infiltration followed by rapid refreezing in the shallow soil.

A similar feature is observed at SLC07 in April 2022, where slight heave is followed by brief subsidence and then renewed slight heave before the onset of sustained thaw settlement. This “shallow trough” in the late-winter deformation record may likewise reflect alternating thawing and refreezing associated with infiltrated water.

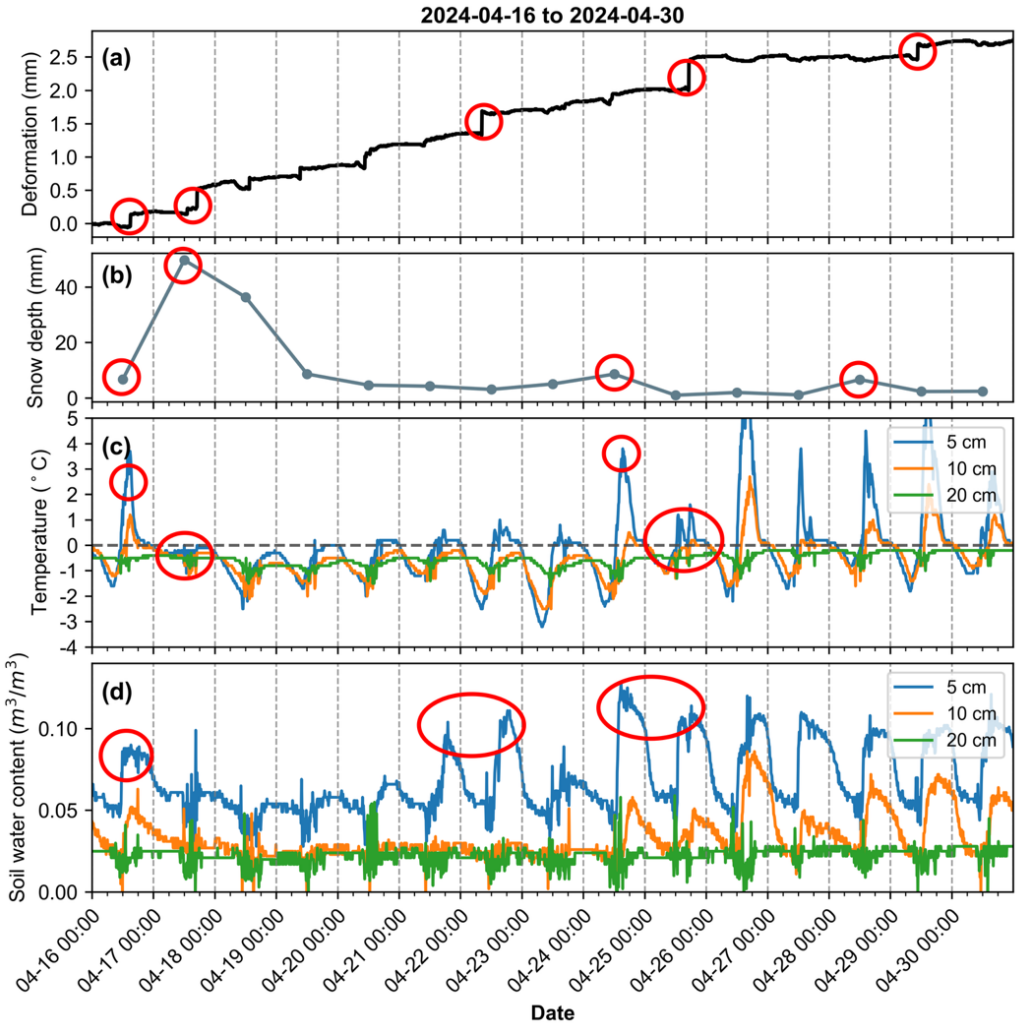


Figure 12. Sub-daily ground surface deformation and concurrent soil temperature and moisture profiles at 5–20 cm depth during 16–30 April 2024. Snow depth was derived from daily raw ultrasonic ranging data and is presented relative to 15 April 2024.